Sustainable Energy & Fuels

ROYAL SOCIETY OF CHEMISTRY

PAPER

View Article Online
View Journal

Cite this: DOI: 10.1039/d5se01657f

Methane synthesis from CO_2 and H_2O with concentrated NaOH–KOH electrolyte at 200–250 °C using electrochemical Pd–Ag membrane reactor

Wakana Seki, Raisei Sagara, Aika Hirata and Jun Kubota *

The synthesis of hydrocarbons from CO_2 and H_2O using electricity derived from renewable energy sources has attracted considerable attention. However, there is currently no direct electrochemical method capable of selectively producing specific hydrocarbons from CO_2 reduction at low overpotentials. By employing an electrochemical membrane reactor that combines water electrolysis with thermocatalytic methanation, methane can be selectively produced at a cell voltage comparable to that of conventional water electrolysis. In this study, methane synthesis from CO_2 and H_2O was investigated using an electrochemical membrane reactor equipped with a 30 wt%-Ru/C catalyst, Pd-based alloy membrane, and a NaOH–KOH eutectic electrolyte operating at approximately 250 °C. At 250 mA cm^{-2} based on cathode geometric area and 250 °C, the methane and hydrogen production rate was 290 and 120 nmol s^{-1} cm^{-2}, corresponding to a current efficiency of 91 and 9%, respectively. However, when the current density exceeded 250 mA cm^{-2}, the total current efficiency suddenly deviated significantly from 100%, indicating a decrease in current efficiency due to product cross-leak. At 300 mA cm^{-2}, significant evolution of H_2 was detected in the anode-side exhaust gas. This cross-leak was also pronounced during operation below 200 °C. Impedance measurements determined that the specific resistance of the electrolyte at 250 °C was 0.50 S cm^{-1}. The current efficiency and related characteristics of this methane synthesis method were discussed in detail.

Received 16th December 2025
Accepted 25th March 2026

DOI: 10.1039/d5se01657f

rsc.li/sustainable-energy

1 Introduction

Achieving a carbon-neutral society requires the establishment of an energy system independent of fossil fuels. At present, there is no doubt that the most practical and abundant alternatives capable of meeting global energy demand are power generation technologies based on hydropower, solar, wind, geothermal, and tidal energies.[1,2] Since these electrical energy sources exhibit significant temporal fluctuations and geographical unevenness across the globe, it is desirable to convert them into chemical fuels.[3–6] Using these electricity sources to convert the large amounts of CO_2 generated from waste incineration or biomass fermentation into fuel can be an effective approach to obtaining carbon-neutral fuels.[3–6] It should be emphasized that, in pursuit of a carbon-neutral society, research on the synthesis of chemical fuels from electrical energy is far more crucial than studies focused on the conversion of chemical fuels into electricity using fuel cells. This is because chemical fuels can generate electricity without the use of fuel cells, utilizing conventional combustion engines and generators with comparable efficiency.[7] In contrast, the synthesis of chemical fuels from electricity can only be achieved through the integration of electrochemistry and catalysis, as purely mechanical systems are incapable of producing fuels.

The electrochemical reduction of CO_2 has long been studied.[8–13] However, a practical method has yet to be established. Electrochemical CO_2 reduction using aqueous or polymer electrolytes near room temperature can selectively produce CO when an Ag cathode is used.[12] While CO serves as a raw material for methanation, methanol synthesis, and Fischer–Tropsch synthesis, CO itself is difficult to consider as a fuel. Using Cu and related-alloy cathodes, CO_2 can be electrochemically converted into hydrocarbons and alcohols.[8–11,13] However, the selectivity for a specific product cannot be increased to a practical level, such as 90%, and the cathodic overpotential is also significant, requiring around −1.5 V_{RHE}, in compare to the hydrogen evolution around 0 V_{RHE}. Here, RHE denotes potentials referenced to the reversible hydrogen electrode. This implies that approximately twice the voltage required for hydrogen production *via* water electrolysis is necessary. Among the possible products, methane[14] or ethylene[15] synthesis *via* electrochemical CO_2 reduction has been reported to achieve a selectivity of around 50–60%. However, from an energy technology perspective, the selectivity and overpotential are unlikely to be sufficient for practical application. Formic acid can frequently be produced with relatively high selectivity. However, in many cases, formate is generated instead of formic acid when

Department of Chemical Engineering, Fukuoka University, 8-19-1, Nanakuma, Jonan-ku, Fukuoka 814-0180, Japan. E-mail: jkubota@fukuoka-u.ac.jp

using a basic electrolyte. In such cases, formate, unlike formic acid, cannot readily be used directly as a hydrogen source. As described above, it is difficult to obtain specific hydrocarbons by reducing CO_2 at an electrochemical interface. In contrast, when a thermocatalytic reaction is employed, the hydrogenation of CO_2 to produce methane, the so-called Sabatier reaction, is one of the relatively simple thermocatalytic reactions with few side reactions.

Against this background, we are working on CO_2 methanation[16–18] and N_2 ammonia synthesis[19,20] in the intermediate temperature range around 200–270 °C by integrating water electrolysis with catalytic hydrogenation reactions using electrochemical membrane reactors. It has been summarized in review articles that electrochemical membrane reactors can perform hydrogenation reactions very effectively.[21] The use of thermocatalysts enables the selective conversion of CO_2 into a variety of hydrocarbons, alcohols, ethers, and so on with high selectivity.[22–26] It has been argued that the direct electrochemical reduction of CO_2 or N_2 is indispensable for efficient conversion. However, in high-temperature solid oxide electrolyte fuel cells, for example, methane or ammonia can be used directly as fuels. In these cases, methane steam reforming, water–gas shift, or ammonia cracking reaction mostly occurs thermocatalytically, rather than electrochemically, at the anode of fuel electrode, generating H_2, which serves as the actual fuel.[27–30] There is no evidence that methane or ammonia undergoes direct electrochemical oxidation, nor is such a process necessary. In electrochemical cells using high-temperature solid electrolytes, the electrodes possess numerous solid–gas interfaces, where electrochemical reactions are impossible to occur. At solid–gas interfaces, faradaic reactions cannot take place because of the absence of an ionically conductive medium required for electrochemical charge transfer. Electrochemical potential is defined only at the interface between an electrolyte and an electrode, and is absent at a solid–gas interface. Instead, thermocatalytic reactions tend to dominate at these interfaces. At intermediate to high temperatures, it is important to combine thermocatalytic reactions with electrochemical reactions occurring at the electrode–electrolyte interface, and direct electrochemical reduction of CO_2 or N_2 is not necessarily indispensable. Our fundamental concept for methane synthesis from CO_2 and H_2O using electricity is based on performing the exact reverse process of that occurring in direct methane-type fuel cells, also known as internal reforming-type fuel cells. It should be noted that this approach does not involve the direct electrochemical reduction of CO_2. Furthermore, it is essential to implement a design that preserves the gas–solid interface required for the thermocatalytic reaction, ensuring that it remains unimpeded by the electrolyte.

Based on this concept, we began researching an electrochemical system for synthesizing methane from CO_2 and water at 270–200 °C. This is because, in electrochemical cells operating above 500 °C, the equilibrium shifts toward the decomposition of methane rather than its formation.[31] We reported a method using a phosphate-based composite electrolyte that enabled methane synthesis at atmospheric pressure with an approximately 95% current efficiency.[16,17] Initially, we used a Pd hydrogen-permeable membrane as the electrode and placed a CO_2 methanation catalyst on the backside.[16] However, a subsequent study reported a method for forming a catalyst layer in which the electrocatalytic region, in contact with the electrolyte, is separated from the thermocatalytic region, where thermal methanation occurs, by employing a polytetrafluoroethylene (PTFE) membrane filter.[17]

Water electrolysis and methane synthesis have also been conducted below 120 °C using fluoropolymer-based solid electrolytes such as Aquivion.[18] A Pd hydrogen-permeable membrane was found to be unnecessary even for the cell utilizing this solid polymer electrolyte. However, when the temperature exceeds 120 °C, the polymer electrolyte undergoes severe degradation, while at 120 °C the reaction rate of the thermocatalytic process remains insufficient.[18]

Phosphate-based electrolytes were considered promising because phosphoric acid fuel cells have already been commercialized, and our electrolyte was a further solidified version of this system. However, a significant issue for water electrolysis was the corrosion of the anode. While stable operation for several weeks was possible at a current density of 10 mA cm^{-2}, degradation occurred within a few hours when the current density was increased to around 50 mA cm^{-2}.[19,20] It has been revealed that anode materials such as Pt/Ti and IrO_2/Pt/Ti do not possess sufficient stability for oxygen evolution under phosphate environments at temperatures above 200 °C.

To address this, we found that for ammonia synthesis, a concentrated solution of NaOH–KOH molten salt electrolyte with added moisture could serve as an effective electrolyte in the 250–200 °C range.[32,33] As far as we are aware, excluding our works, no studies have been reported on the synthesis of methane or ammonia with water electrolysis in an electrochemical membrane reactor employing a Pd-alloy hydrogen-permeable membrane to separate the catalytic reaction zone with a molten NaOH–KOH electrolyte. This concept was further extended to methanation in the present study. Fig. 1 shows a schematic illustration of the electrochemical membrane reactor, in which the chemical reaction equations at each

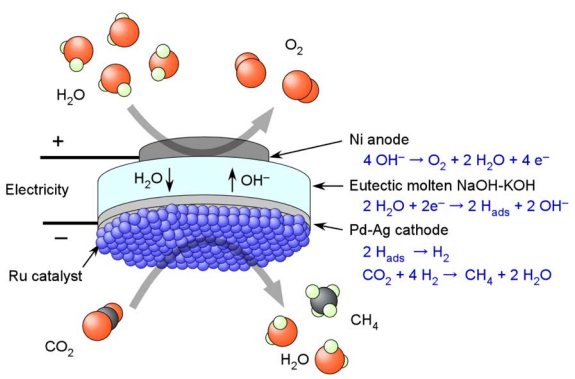

Fig. 1 Schematic representation of an electrochemical membrane reactor using a eutectic molten NaOH–KOH electrolyte and a Ru-based methanation catalyst. The chemical reaction equations at each interface are shown.

surface are indicated. When attempting the electrochemical reaction of CO_2 in an alkaline electrolyte, CO_2 is normally absorbed by the electrolyte and converted to carbonate. However, in the present cell, the Pd–Ag hydrogen-permeable membrane completely blocks CO_2 permeation, preventing the formation of carbonates in the alkaline electrolyte. The Ni electrode appears to exhibit sufficient resistance to the NaOH–KOH electrolyte, and no degradation of the electrochemical cell was observed during a test period of approximately one month.[33] Therefore, in this paper, we demonstrate the possibility of using NaOH–KOH molten salt as an electrolyte for CO_2 methanation. The objective of this study is not to identify a fundamentally new reaction pathway, but to propose a simple and efficient approach for synthesizing methane from CO_2 and water.

2 Experimental

The sectional view of the methane synthesis cell is shown in Fig. 2A. The methanation catalyst consisted of 0.20 g of 30 wt%-Ru/C. A Pd–Ag membrane (75 : 25 atomic ratio), 0.10 mm thick with an active area of 20 mm in diameter, was employed as both the cathode and hydrogen-permeable membrane. A mixture of 0.20 mol NaOH and 0.20 mol KOH was dissolved in 20 mL of H_2O, and approximately 5 mL of this solution was introduced into the cell. The anode was a Ni disk with a diameter of 10 mm and a thickness of 5.0 mm. The anode vessel of the cell was fabricated from Ni, whereas the cathode vessel was made of stainless steel. The gasket between the anode and cathode vessels was a foam made of PTFE (GORE Hypersheet, Gore Japan), which is reported to be usable over the temperature range from −240 to 315 °C in the manual. Although the diameter of the Ni anode disk was 10 mm, the side surface of the disk is also exposed to the electrolyte, making the precise electrode area indeterminate. As described in the first section of the results and discussion, the NaOH–KOH electrolyte absorbs water upon humidification, and its volume varies depending on the conditions, making it difficult to determine the exact configuration inside the cell. When only the end face is in contact, the anode electrode area is 0.79 cm^2; however, it is highly likely that the side surface also contacts the electrolyte, giving a total electrode area of 2.4 cm^2 when both the end and side surfaces are considered. Owing to the cell structure, the effective anode area therefore lies flexibly between these values. Therefore, given that the active area of the Pd–Ag cathode in contact with the electrolyte was a 20 mm diameter surface (3.14 cm^2), the electrode area of the cell was defined based on the cathode area. Accordingly, the electrode area used to determine the current density, formation rate, and gas flow rate was normalized to 3.14 cm^2.

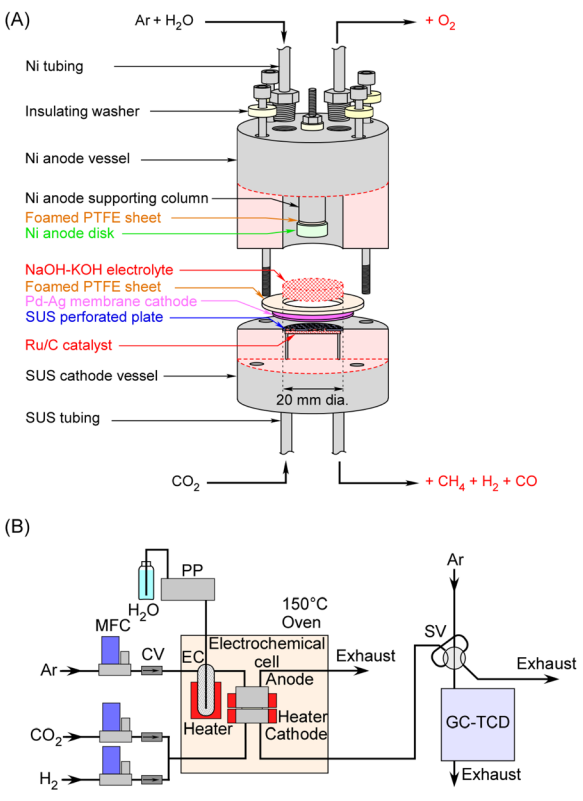

Fig. 2 Cross sectional illustration of electrochemical membrane reactor (A) and process flow diagram of methanation (B). The abbreviations are as follows: stainless steel (SUS), polytetrafluoroethylene (PTFE), plunger pump (PP), mass flow controller (MFC), check valve (CV), evaporation chamber (EC), sampling valve (SV), and gas chromatograph equipped with a thermal conductivity detector (GC-TCD).

Ru/C catalysts were employed in this study because, due to their conductive support, they are considered suitable for the future design of catalyst layers integrating both electrocatalytic and thermocatalytic functions. The Ru/C catalyst was prepared from tetrahydrofuran solution of $Ru_3(CO)_{12}$ (TANAKA Kikinzoku Kogyo K.K.). A carbon black (Vulcan XC-72R, Cabot Co.) powder was immersed in the tetrahydrofuran solution of $Ru_3(CO)_{12}$ for 4 h at room temperature, followed by removal of the solvent using a rotary evaporator under reduced pressure at temperature below 40 °C. The resulting $Ru_3(CO)_{12}$/C was decomposed under vacuum at 400 °C and subsequently reduced under a H_2 flow at 400 °C.

The process flow diagram is illustrated in Fig. 2B. CO_2 at a predetermined flow rate was supplied to the cathode side, while Ar and liquid water were introduced to the anode side after being vaporized through an evaporation chamber. The flow rates of the gases were controlled using mass flow controllers, and the water flow rate was regulated using a plunger pump. The gas flow rate was expressed as the volumetric flow of gas at standard temperature and pressure (STP; 0 °C and 101.3 kPa) per minute per unit electrode area (3.14 cm^2) of the cell as mL_{STP} min^{-1} cm^{-2}. The cathode exhaust gases were analyzed using a gas chromatograph (Model 4200, GL Sciences Inc.) equipped with a thermal conductivity detector (GC-TCD). Methane production rates were calculated from the peak area ratios in the gas chromatograph traces, assuming a carbon balance with respect to the CO_2 feed rate. That is, the amount of by-produced H_2 is quantified such that the total amount of CH_4, CO, and CO_2 exiting the electrochemical cell equals the amount of CO_2 introduced.

The CH_4 formation rate was determined based on the carbon balance between the inlet CO_2 and the carbon-containing products detected in the outlet gas. Because this approach relies on gas chromatographic quantification and the assumption that the major carbon-containing products are detected, the calculated methane formation rate contains an uncertainty associated with the analytical precision of the gas analysis and possible undetected minor products. Therefore, the quantitative values reported here should be interpreted within the uncertainty inherent to the carbon-balance-based analysis. For this reason, the formation rates of CH_4, H_2, and other products are calculated from the inlet flow rate of CO_2, and therefore uncertainties in the CO_2 inlet flow rate strongly affect the calculated formation rates. In the present study, the CO_2 flow rate was at a level below 1 mL_{STP} min^{-1}, and it should be recognized that flow rates in this range may contain errors of approximately 1–10% even when measured using a mass flow controller.

This approach relies on the assumptions that there is no gas leakage from the system and that no carbon-containing products other than CH_4, CO, and the feed CO_2 are present. However, from a thermodynamic standpoint, the formation of other carbon-containing products in the Sabatier reaction is unlikely, and numerous previous studies support this understanding.[31]

Detailed descriptions of the gas chromatograph sensitivity and calculation methods are provided in the SI. In addition, the SI includes results showing that no methane was produced in the absence of the catalyst. Photographs of the actual apparatus corresponding to Fig. 2 are provided in Fig. S2 of the SI.

Although the sum of the current efficiencies of each product does not always exactly equal 100%, the experimental uncertainty in the present study is on the order of ±10% for each value. This uncertainty mainly arises from the limited accuracy of the CO_2 flow rate, which serves as the basis for all formation rate calculations and is only accurate to approximately ±10% at such low flow rates. Consequently, a small deviation of the total current efficiency from 100% is considered to fall within the experimental error.

For reference, when the cell was operated without loading Ru/C and the cathode side consisted only of a Pd–Ag membrane, hydrogen was the only electrochemically generated product, and the outlet gas contained only the feed CO_2 and H_2. The examples of original gas chromatograms for this experiment are provided in SI. In addition, the linearity of the GC sensitivity and a table of the response factors for each gas are also provided in the SI.

Electrochemical impedance measurements were carried out using an electrochemical measurement system equipped with an impedance analyzer (HZ-7000, Meiden Hokuto Co.).

The transmission electron microscope (TEM) measurements were performed with JEM-2100, JEOL Ltd at Analytical Instrument Facility, Graduate School of Science. The University of Osaka. X-ray diffraction (XRD) measurements were performed with XRD-6100, Shimadzu Co.

3 Results and discussion

3.1 NaOH–KOH electrolyte

The NaOH–KOH electrolyte employed in this electrochemical cell is described, as in our previous literature. NaOH and KOH have melting points of 318 °C and 360 °C, respectively; however, a eutectic mixture consisting of 51.5 mol% NaOH and 48.5 mol% KOH exhibits a significantly reduced melting point of approximately 170 °C. In this electrochemical cell, the electrolyte is exposed to the anode gas, which consists of a mixture of Ar at 10 cm_{STP}^3 min^{-1} and liquid H_2O supplied at 5 μL min^{-1}, corresponding to a steam concentration of 38 vol%. According to the literature, the Henry constant of water vapor in the NaOH–KOH mixture is reported to be 0.0095 atm mol^{-1} kg at 250 °C.[34,35] Under atmospheric pressure, when the anode gas described above is supplied, it is estimated that water corresponding to 72% of the mass of the NaOH–KOH mixture is dissolved in the NaOH–KOH mixture. The NaOH–KOH eutectic mixture remains in a molten state above 170 °C; however, it is presumed that under the present operating conditions it simultaneously absorbs humid steam, resulting in the formation of a highly concentrated aqueous phase. Electrochemical cells utilizing NaOH or KOH at around 200 °C have been reported in several studies.[36,37]

The NaOH–KOH electrolyte exhibits very little degradation when a Ni anode is used; however, it should be noted that there is an intrinsic issue in methane synthesis from CO_2 and H_2O. Because CO_2 is an acidic gas, it is absorbed into the NaOH–KOH electrolyte and neutralizes it, which necessitates the use of a Pd alloy hydrogen-permeable membrane. Since Pd is a rare material, in methane synthesis from CO_2 and H_2O, phosphate electrolytes have been used in combination with hydrophobic PTFE membrane filters instead of Pd-alloy membranes, and polymer electrolyte systems have been developed without membrane separation.[17] These approaches were feasible because the electrolytes were acidic. In contrast, for the present alkaline NaOH–KOH electrolyte, the use of a Pd alloy hydrogen-permeable membrane is indispensable to completely prevent the absorption of CO_2 into the electrolyte.

3.2 Temperature dependence

The temperature dependence of rate of formation of methane between 90 and 250 °C at 50 mA cm^{-2} based on cathode geometric area was examined as shown in Fig. 3. The numerical data underlying this graph are provided in SI. At 250 °C, rate of formation of methane and hydrogen were 61.9 and 10.0 nmol s^{-1} cm^{-2}, respectively, which corresponding to the current efficiencies of 95.5 and 3.9% respectively. No carbon monoxide was detected at this temperature. The deviation of the sum of 95.5% and 3.9% from 100% was attributed to experimental error.

At this point, it is necessary to define the current efficiency. The current efficiencies for methane, hydrogen, and carbon monoxide (CE_{CH_4}, CE_{H_2}, and CE_{CO}, respectively), expressed as percentages, are defined by the following equations. The current efficiency for methane synthesis *via* CO_2 hydrogenation

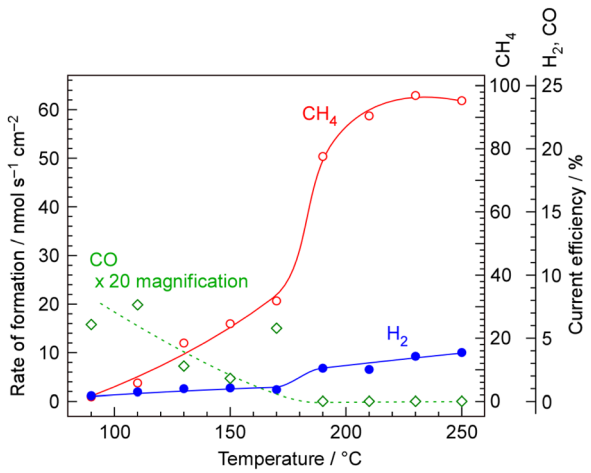

Fig. 3 Formation rate of CH_4, H_2, and CO, along with their respective current efficiencies, as a function of temperature. A secondary axis was added on the right to indicate the current efficiency. The current density was 50 mA cm^{-2}, and the CO_2 flow rate was 0.088 mL$_{STP}$ min^{-1} cm^{-2}. All currents, formation and flow rates are normalized to the cathode geometric area. Based on cathode geometric area.

is calculated based on an eight-electron reaction; it is not defined on the basis of allocating four electrons to produced methane and four electrons to produced water, for example.[16–18]

$$CE_{CH_4} = \frac{8 \times F \times r_{CH_4}}{j} \times 100 \quad (1)$$

$$CE_{H_2} = \frac{2 \times F \times r_{H_2}}{j} \times 100 \quad (2)$$

$$CE_{CO} = \frac{2 \times F \times r_{CO}}{j} \times 100 \quad (3)$$

where r_{CH_4}, r_{CO}, and r_{H_2} are rates of formation of methane, hydrogen, and carbon monoxide, respectively, in mol cm^{-2} s^{-1}. F and j are faradaic constant (96 500 s A mol^{-1}) and current density in A cm^{-2}, respectively. The current efficiency is often referred to as the faradaic efficiency; however, in this electrochemical membrane reactor, the products are not directly formed through charge–transfer reactions (Faradaic reactions), and therefore the term of faradaic efficiency was not used.

At 250 and 230 °C, CE_{CH_4} and CE_{H_2} were about 96 and 4%, respectively. The thermodynamic equilibrium conversion of CO_2 to methane in the stoichiometric ratio of reactant is 97%, indicating that the reaction has nearly reached the equilibrium. However, with decreasing temperature from 210 to 150 °C, CE_{CH_4} was drastically decreased. If the catalytic reaction rate is insufficient to produce methane at low temperatures, the formation of unreacted H_2 should increase compensatorily; however, CE_{H_2} also decreases. In other words, at temperatures below 210 °C, the overall current efficiency decreased with decreasing temperature, indicating that the electrochemical membrane reactor does not function properly under these conditions.

In addition, carbon monoxide began to be detected among the products below 170 °C, and its formation rate increases as the temperature decreases. Although thermodynamic equilibrium does not allow the presence of CO at such low temperatures, the insufficient catalytic reaction rate suggests that CO is released as an intermediate formed during the hydrogenation of CO_2. Because CO is not detected at elevated temperatures, it is clear that the catalytic activity is insufficient under the conditions where CO formation is observed.

The overall current efficiency deviates from 100% below 210 °C, indicating that the electrochemical membrane reactor with the NaOH–KOH electrolyte does not operate properly under these conditions. In the temperature range of 150–200 °C, the electrolyte approaches its melting point and is therefore considered to lose its ability to effectively separate the anode and cathode due to changes in viscosity. Without the gas-tightness provided by the liquid phase between the anode and cathode, the oxygen generated at the anode can easily migrate to the cathode as a cross-leak, where it reacts with hydrogen in the Pd alloy, resulting in a decrease in the overall current efficiency. Conversely, H_2 that is not absorbed into the Pd–Ag membrane cathode does not permeate to the catalyst layer side but is released to the electrolyte side, which also constitutes one of the causes of cross-leakage. Cross-leakage is discussed in Section 3.6.

3.3 Current density dependence

Fig. 4 shows the behaviors of the formation rates and current efficiencies of methane and hydrogen with increasing current density at 250 °C. The numerical data underlying this graph are provided in SI. The formation rates of both methane and hydrogen increased monotonically with increasing current density up to 250 mA cm^{-2}, based on cathode geometric area. With respect to current efficiency, CE_{CH_4} slightly decreased from 97% at 50 mA cm^{-2} to 91% at 250 mA cm^{-2}. Conversely, CE_{H_2} increased from 5.1% to 9.0% with increasing current density, showing a compensatory relationship. Thus, it was found that the overall current efficiency remained nearly 100% up to 250 mA cm^{-2}, and the slight decrease in CE_{CH_4} with increasing current density was attributed to insufficient catalytic activity.

When the current density exceeded 250 mA cm^{-2}, further increases did not result in higher formation rates of either methane or hydrogen. Correspondingly, the current efficiencies for both products decreased, leading to a deviation of the overall current efficiency from 100%. Such a deviation indicates that either cathode-generated products were transported to the anode and consumed, or anode-generated products were transported to the cathode and consumed. It is reasonable to attribute this behavior to the phenomenon known as cross-leakage or crossover. Two possible explanations can be considered: either oxygen bubbles generated at the anode reached the cathode, or the Pd alloy hydrogen-permeable membrane could not fully absorb hydrogen, resulting in hydrogen evolution on the electrolyte side. The issue of cross-leakage is discussed in Section 3.6.

3.4 Current–voltage properties

Before discussing the issues related to cross-leakage, we would like to first address the electrical characteristics of the cell and

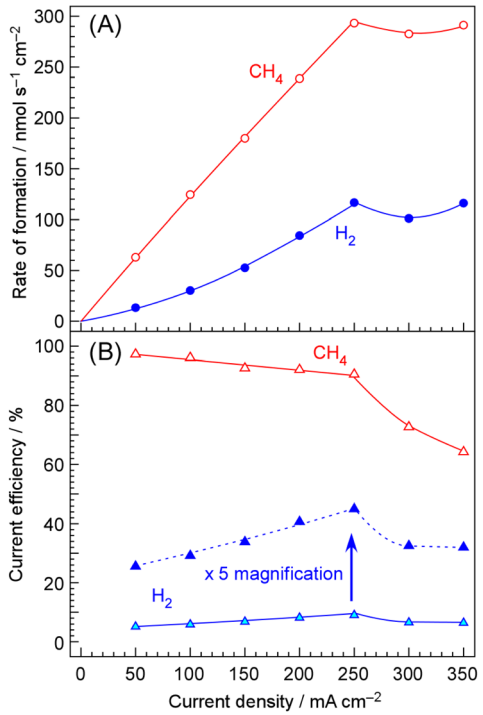

Fig. 4 Formation rate of CH_4 and H_2 (A), along with their respective current efficiencies (B), as a function of current density. For clarity, the current efficiency of H_2 is also shown with a fivefold magnification. The temperature was 250 °C and the CO_2 flow rate was proportional to the current density, with a ratio of 0.18 mL_{STP} min^{-1} cm^{-2} per 100 mA cm^{-2}. All currents, formation and flow rates are normalized to the cathode geometric area. Based on cathode geometric area.

the electrolyte resistance. Time courses of cell voltage at various current densities are shown in Fig. 5A. The electrochemical cell was operated in the constant-current mode using a power supply. The time-averaged cell voltages are plotted against current density in Fig. 5B. As shown in Fig. 4, when the current density exceeded 250 mA cm^{-2} based on cathode geometric area, the current efficiencies for methane and hydrogen suddenly ceased to increase, and the total current efficiency deviated from 100%. However, no abnormality was observed in the current–voltage characteristics beyond 250 mA cm^{-2}.

The cell voltage remained stable over 180 min regardless of the current density. It has also been reported that a similar cell can operate stably for approximately 30 days. However, at a current density of 250 mA cm^{-2} based on cathode geometric area, the cell voltage was 3.2 V, which is nearly three times higher than the thermodynamic equilibrium cell voltage (1.02 V) calculated from the standard Gibbs free energy of reaction (ΔG_r°), assuming that both the reactants and products are in the gaseous phase. For detailed values of the thermodynamic parameter such as (ΔG_r°) and (ΔH_r°), we would like to refer the reader to our earlier work.[17]

At current densities up to 100 mA cm^{-2}, the cell voltage remains below 1.8 V. The standard enthalpy change (ΔH_r°) for methane synthesis from CO_2 and H_2O corresponds to 1.17 V, indicating that a cell voltage of 1.8 V yields a voltage efficiency of

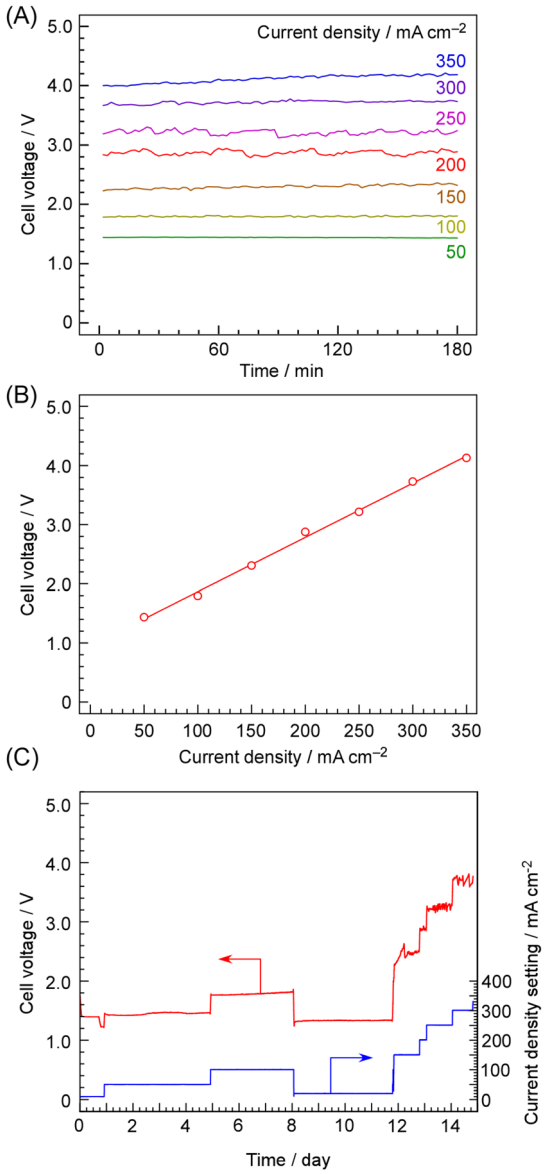

Fig. 5 Time courses of cell voltage at various current densities (A), and time-averaged cell voltage plotted against current density (B). The long-term cell voltage during 15 days of operation at various current densities is shown in (C). The cell temperature was 250 °C. The current density was defined as based on cathode geometric area.

65%. Because the calculations are based on ΔH_r°, water is treated as liquid water in the energy balance, and the values therefore correspond to the higher heating value (HHV). Given that the current efficiency at 100 mA cm^{-2} based on cathode geometric area is 95%, the overall gross energy efficiency for converting CO_2 to methane reaches 62%. This energy efficiency is based on physicochemical considerations derived from the electrical power input and methane production, and does not account for the energy required for cell heating or the energy required for methane liquefaction.

Methane synthesis from CO_2 and H_2O can be described as a two-step process consisting of water electrolysis followed by the Sabatier reaction. Because the Sabatier reaction is

exothermic, its apparent energy efficiency can exceed 100% when the released heat is recovered and utilized. Consequently, the overall process efficiency is effectively governed by the energy efficiency of the water electrolysis step. The efficiency of water electrolysis has been widely summarized in the literature.[38,39] Reported efficiencies are 62–82% (HHV) for alkaline electrolysis and 67–84% for polymer electrolyte membrane (PEM) electrolysis in the literature.[38] The methane synthesis efficiency obtained in this study almost falls within this range, demonstrating that methane can be produced with an efficiency comparable to that of hydrogen production by water electrolysis.

Fig. 5B shows a linear relationship between current density and cell voltage. If the activation overpotential were dominating the cell voltage, current density and cell voltage should follow the Tafel equation and thus exhibit an exponential relationship. Therefore, the overpotential with respect to the theoretical equilibrium potential is unlikely to be largely due to activation overpotential.

An example of the long-term cell voltage during 15 days of operation at various current densities is shown in Fig. 5C. Although some minor fluctuations in the cell voltage were observed, no significant variations attributable to cell degradation were detected. Although some minor fluctuations in the cell voltage were observed, no significant variations attributable to degradation of the electrochemical properties were detected. However, the deterioration of the methane formation rate over the catalyst was not evaluated in this study and remains a subject for future investigation. While this was in the context of ammonia synthesis, we have previously reported stable operation for 28 days using an electrochemical cell with an identical structure,[33] demonstrating that this electrolyte and these electrodes are not merely able to withstand short-term experiments of two or three days, as is often the case in university laboratories.

3.5 Impedance measurements

In order to elucidate the origin of the high overpotential observed at current densities above 100 mA cm^{-2} based on cathode geometric area, electrochemical impedance spectroscopy (EIS) measurements were performed on the cell. The obtained Nyquist plots at 1.0 and 1.2 V of cell voltage at 250 °C are presented in Fig. 6. As is clear from the applied voltage conditions, the EIS measurements were conducted to determine the conductivity of the electrolyte and were performed at low voltages, not under the conditions used for methane synthesis. This was done to evaluate the electrolyte conductivity under conditions free from the influence of bubbles or other effects. The solid lines in the figure represent the fitted curves obtained using the equivalent circuit composed of resistors and constant phase elements (CPE), as also shown in Fig. 6.[40] The detailed fitting parameters of EIS are provided in Table 1. The cell consists of two electrodes, an anode and a cathode, and it is difficult to assign the resistance of R_1 and R_2 and CPE_1 and CPE_2 in the Nyquist plot to specific parts of the cell. While these R and CPE undoubtedly reflect information on reaction kinetic

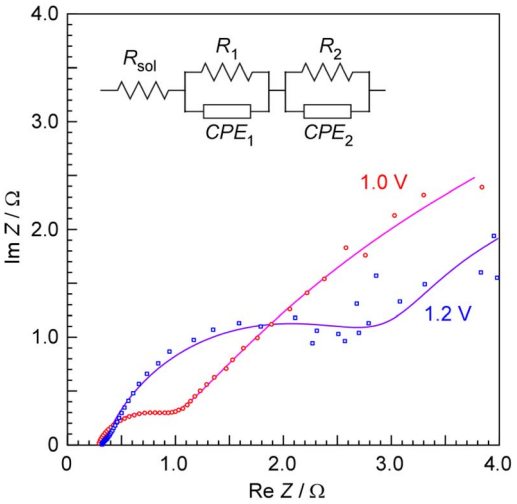

Fig. 6 Nyquist plots of the methane synthesis cell at 250 °C under cell voltages of 1.0 and 1.2 V. The solid lines represent the fitted curves obtained using the equivalent circuit shown in the figure. R and CPE represent the resistance and constant phase element.

resistances and electric double layers at both the anode and cathode, accurate assignment is challenging without conducting separate half-cell measurements using a three-electrode setup. Thus, only the solution resistance of the electrolyte could be assigned with certainty. The solution resistance (R_{sol}) was nearly identical at cell voltages of 1.0 and 1.2 V, with values of 0.304 and 0.336 Ω, respectively. The average solution resistance was 0.32 Ω, and assuming an electrode area of 3.14 cm^2 and an inter-electrode distance of 0.5 cm, the specific conductivity of the electrolyte was calculated to be approximately 0.5 S cm^{-1}. Indeed, in this cell it is difficult to define the anode area accurately, and it is also unclear to what extent the side surface of the anode is in contact with the electrolyte. For these reasons, the conductivity has been discussed only as an approximate value, on the order of 0.5 S cm^{-1}, with a precision of roughly one significant figure.

The absence of suitable electrolytes in the 200–400 °C range is referred to as the Norby gap,[41] and many electrochemical systems operating in this temperature range are still under development.[42] Indeed, in fuel cells, the advantage of solid electrolytes is evident for maintaining efficient triple-phase boundary. However, in electrolysis, where the reactants are

Table 1 Parameters of the equivalent circuit fitted to the Nyquist plots in Fig. 6

Volt	R_{sol}	R_1	CPE_1		R_2	CPE_2	
V	Ω	Ω	T^a	α^a	Ω	T^a	α^a
1.0	0.304	0.500	0.00273	0.957	35.2	0.235	0.543
1.2	0.336	1.41	0.157	0.773	4.15	0.858	1.00

[a] The impedance of a CPE is given by $Z_{CPE} = 1/[T(j\omega)^{\alpha}]$ where j and ω denote the imaginary unit and the angular frequency. The parameters T and α are summarized in this table.

liquids and the products are gases, there is less need to insist on solid-state electrolytes as in fuel cells. The electrolyte used in this study exhibited a conductivity of 0.5 S cm^{-1} at 250 °C, which lies within the so-called Norby gap, indicating that it possesses a sufficiently high ionic conductivity. As in industrial hydrogen production *via* alkaline water electrolysis, the usefulness of liquid electrolytes is well established.

If the solution resistance was 0.32 Ω, the voltage drop across the electrolyte was estimated to be 0.050–0.35 V for cell currents of 157–1099 mA (50–350 mA cm^{-2}). This voltage drop is negligibly small compared to the cell voltage shown in Fig. 5B, indicating that the solution resistance does not dominate the high voltage observed at higher current densities. At current densities of several hundred mA cm^{-2}, a large amount of oxygen bubbles is expected to be generated during electrolysis, and the detachment of bubbles from the electrode is likely to constitute a significant resistance factor. In this study, planar electrodes were used; however, the incorporation of porous electrodes such as Ni foam will be necessary in the future to reduce overpotentials under high current density conditions.

3.6 Discussion in the cross-leakage

The phenomenon in which the overall current efficiency does not reach 100% when the temperature is lowered below 200 °C or when the current density exceeds 250 mA cm^{-2} is considered to be due to so-called cross-leakage. Two possible explanations can be considered: either oxygen bubbles generated at the anode reached the cathode, or the Pd alloy hydrogen-permeable membrane could not fully absorb hydrogen, resulting in hydrogen evolution on the electrolyte side.

Therefore, the hydrogen permeability of Pd–Ag is first estimated based on previously reported permeability data, followed by a description of the results of the analysis of the gas on the anode side.

3.6.1 Hydrogen permeability. One possible reason for the decrease in overall current efficiency below 210 °C or above 250 mA cm^{-2} based on cathode geometric area is the limited hydrogen permeation through the Pd–Ag membrane. Therefore, the hydrogen permeability was discussed as follows.

The hydrogen permeation through a Pd–Ag (75–25% atomic ratio) membrane between 150–300 °C was reported in a literature.[43] The hydrogen flux due to diffusion obeys the following equation.[44]

$$J = \frac{P_e}{d}\left(\sqrt{p_1} - \sqrt{p_2}\right)$$

where J is the hydrogen flux in mol m^{-2} s^{-1}, P_e is the permeability in mol m^{-1} s^{-1} $Pa^{-0.5}$, d is the membrane thickness in m, and p_1 and p_2 are hydrogen partial pressures in Pa at the hydrogen absorption and desorption interfaces, respectively. P_e is also the product of the solubility coefficient and the diffusion coefficient. From the experimental results reported in reference,[43] the permeability P_e was averagely determined to be 2.16×10^{-8}, 1.55×10^{-8}, and 8.29×10^{-9} mol m^{-1} s^{-1} $Pa^{-0.5}$ at 250, 200, and 150 °C, respectively.

In this experiment, since the hydrogen conversion is approximately 90%, p_1 and p_2 are assumed to be 101.3 and 10.13 kPa, respectively, and the membrane thickness is taken as 0.10 mm. From these values, the hydrogen fluxes were calculated to be 0.047, 0.034, and 0.018 mol m^{-2} s^{-1} at 250, 200, and 150 °C, respectively. When expressed per cm^{-2}, these values correspond to 4.7, 3.4, and 1.8 μmol cm^{-2} s^{-1}, respectively. However, this calculation is based on the simplest diffusion model, and some deviation should be expected when effects such as surface resistance are also taken into account.[43,44]

In Fig. 4, the production rate of methane at 250 mA cm^{-2} based on cathode geometric area reaches 290 nmol s^{-1} cm^{-2}, which corresponds to a consumption of 1160 nmol s^{-1} cm^{-2} of hydrogen. Since the hydrogen flux through the Pd–Ag membrane calculated at 250 °C is approximately four times higher. Therefore, at that stage, it was considered that there was still some margin in the permeability of Pd–Ag.

3.6.2 Anode gas analysis. The GC-TCD that had been connected to the cathode side was reconnected to the anode exhaust to analyse the gas from the anode side. A large amount of H_2O for water electrolysis was introduced to the anode side, so the exhaust gas was analysed after condensing and trapping the H_2O at room temperature. The carrier gas for the anode H_2O vapor was Ar, but since the GC carrier gas was also Ar, it was not detected. Only O_2 and H_2 were detected, and the amounts of H_2 relative to O_2 at various current densities are shown in Fig. 7.

First, at 50 and 100 mA cm^{-2}, slightly less than 1% of H_2 relative to O_2 was detected. However, at 300 mA cm^{-2}, as much as 47 percent of H_2 relative to O_2 was detected from the anode side.

As shown in Fig. 4, at 300 mA cm^{-2} the overall current efficiency on the cathode side was more than 20% short of 100%, indicating a significant deficit. It was therefore concluded that this deficiency was due to the release of H_2 from the anode side. Although H_2 in the anode exhaust amounted to as much as 47% relative to O_2, if part of the H_2 and O_2 recombined and the current efficiency for O_2 was therefore less than 100%, this

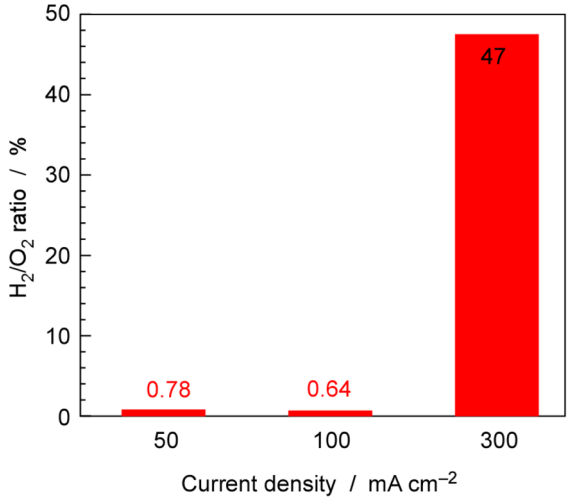

Fig. 7 GC analysis of the anode exhaust gas for the current density at 50, 100, and 300 mA cm^{-2} at 250 °C. The current density was defined as based on cathode geometric area. The fraction of H_2 when the amount of O_2 is taken as 100%.

amount can be considered to correspond to the deficit observed on the cathode side.

In the previous section, we estimated the hydrogen permeability of the Pd–Ag membrane and suggested that there was sufficient margin in the hydrogen permeation rate. However, in practice, at current densities exceeding approximately 250 mA cm^{-2}, H_2 evolution was observed on the electrolyte side of the membrane, suggesting that the hydrogen permeation rate may approach its practical limit under these conditions.

In the earlier estimation, the H_2 partial pressure in the catalyst layer was assumed to be 10.13 kPa, based on an H_2 conversion of approximately 90% for CH_4 synthesis. In reality, however, H_2 could accumulate on the catalyst-layer side of the Pd–Ag membrane surface, which may lead to a higher H_2 partial pressure than that assumed in the calculation. Alternatively, it is also possible that the effective permeation rate was reduced due to contamination or surface modification of the Pd–Ag membrane.

The presence of H_2 in the anode exhaust, which consists mainly of O_2, poses a significant safety concern and must be avoided. At the laboratory scale, there is no major safety issue if the anode gas is promptly vented to the atmosphere. However, for practical-scale systems, it is necessary to construct a system that prevents such conditions from occurring. If the H_2 level is below 1% in the current efficiency, as in the case of current densities of 100 mA cm^{-2} or less, it is considered that the issue would not be serious.

3.7 Comparison to our previous studies

We summarized our previous studies combining water electrolysis and methanation in Table 2. Instead of aiming for methanation through direct electrochemical CO_2 reduction, there are very few studies that take the perspective of integrating catalytic methanation with water electrolysis under the same temperature and pressure, with the goal of proposing a practical device. In principle, the performance of methanation primarily depends on the catalytic activity of the catalyst layer, and thus is largely independent of the electrolyte used. Similar methanation activity has been observed for Ru/ZrO_2, Ru/Al_2O_3, and Ru/C catalysts, whereas Ru/TiO_2 exhibits lower methane formation rates, indicating that careful selection of the Ru catalyst support is required.[16–18]

Solid polymer membranes, such as those used in polymer electrolyte membrane (PEM) water electrolysis, can be expected to function similarly; however, operation at 120 °C results in significant degradation, yielding only approximately 70% methane current efficiency at 30 mA cm^{-2}, highlighting that the temperature is insufficient. For phosphate electrolytes, although noble metal anodes such as Pt are employed, the

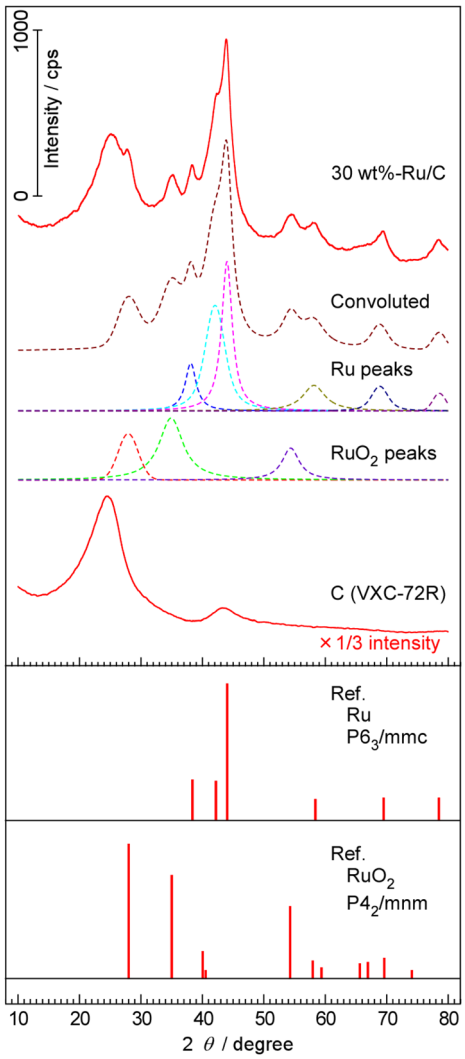

Fig. 8 XRD patterns of 30 wt%-Ru/C and carbon support. Dashed lines are deconvoluted peaks to the diffraction patterns of Ru and RuO_2. Reference patterns were obtained from ref. 45.

Table 2 Comparison to our previous studies using phosphate and polymer electrolytes for methane synthesis

Electrolyte	Phosphate	Polymer	NaOH–KOH
Typical operation temperature (°C)	250	120	250
Electrolyte state	Liquid/Solid	Solid	Liquid
Anode	Pt/Ti	IrO_2/PtTi	Ni
CE_{CH_4} (%)[a]	95	70	95
Life time	A few weeks	~1 week	>1 month[33]
Degradation	Anode	Electrolyte	Not detected
Ref.	16 and 17	18	This work

[a] At 30 mA cm^{-2}.

leaching of Ti-based substrates is severe, leading to a rapid increase in cell voltage after 2–3 weeks of operation, ultimately preventing stable operation.

Considering these factors, the NaOH–KOH eutectic molten salt electrolyte currently offers significant advantages.

3.8 Catalyst characterization

XRD and TEM analyses were conducted for the Ru/C catalyst. The XRD patterns of the 30 wt%-Ru/C sample and the carbon support are shown in Fig. 8. Broad features at 25° and 43° were observed for both Ru/C and the carbon support, corresponding to diffraction from carbon black containing graphitic crystallites. In addition, intense diffraction peaks at 38.4, 42.2, 44.0, 58.4, 69.5, and 78.5° were observed for Ru/C, which were assigned to the (100), (002), (101), (102), (110), and (103) planes of hexagonal Ru metal, respectively.[45] These six peaks were deconvoluted, and the full width at half maximum (FWHM) of respective peaks were estimated. The crystallite size was estimated using the Scherrer equation, as shown below.[46]

$$D = \frac{K\lambda}{\beta \cos \theta} \quad (4)$$

where, D is the crystallite size in nm, K is the Scherrer constant (0.900), λ is the X-ray wavelength (0.154 nm, Cu Kα), β is the FWHM of peaks in radians, and θ is the Bragg angle in radians. From the Bragg angles and FWHM of respective peaks, the crystallite size was calculated to be 2.1–4.1 nm, and the average crystallite size was estimated to be approximately 3.1 nm.

The peaks at 28.0, 35.0, and 54.3° were assigned to RuO_2.[45] Because the 30 wt%-Ru/C sample was handled in air before XRD measurements, and a portion of Ru nanoparticles is considered to have been oxidized to RuO_2 when the reduced sample was taken out into the ambient air. Literature reports indicate that oxidized Ru species can be reduced by H_2 at approximately 200 °C.[47,48] This suggests that the observed RuO_2 likely formed upon exposure of the catalyst to air. During operation of the present electrochemical cell, the catalyst is continuously exposed to a hydrogen-containing reducing environment, and thus RuO_2 is expected to be reduced to metallic Ru.

The TEM images of 30 wt%-Ru/C and carbon support are shown in Fig. 9. The bright spherical particles with a diameter of approximately 30–40 nm correspond to carbon black, whereas the dark particles with diameters of approximately 3 nm correspond to Ru metal. Since the crystallite size described above is consistent with the size of the Ru particles, the particles observed in the TEM images can be considered representative of the average particle size.

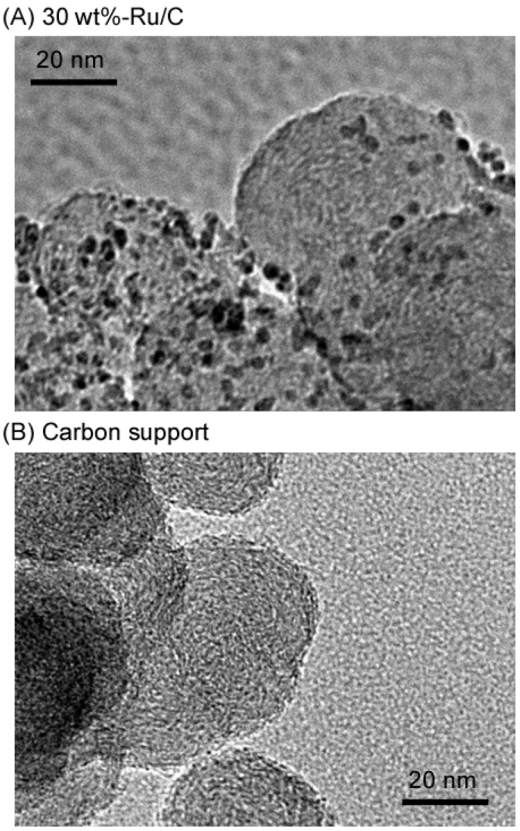

Fig. 9 TEM images of 30 wt%-Ru/C (A) and carbon support (B).

4 Conclusions

A method for synthesizing methane from CO_2 and H_2O at 250 °C using a NaOH–KOH electrolyte in an electrochemical Pd–Ag membrane reactor was proposed in this work. At 250 °C and a current density of 250 mA cm^{-2} based on cathode geometric area, the current efficiency for methane formation reached 91%, demonstrating that methane can be produced much more efficiently than by direct electrochemical reduction of CO_2. Although the cell voltage remains below 2 V at current densities up to approximately 100 mA cm^{-2} based on cathode geometric area, it increases linearly at higher current densities, and the reduction of this overpotential remains a challenge for future work. The electrolyte exhibited a high conductivity of 0.5 S cm^{-1} at 250 °C, superior to other electrolytes used in this temperature range, such as phosphate-based electrolytes. The hydrogen permeation rate of the Pd alloy membrane was estimated, suggesting that it is sufficient to sustain the applied current densities.

Author contributions

Seki and Hirata mainly carried out the material synthesis and routine experimental procedures, and calculated the formation rate and current efficiency from the results. Sagara ensured the proper operation of the experimental apparatus and took responsibility for the assembly of the cells and piping, thereby carrying out the experiments reliably. Kubota assumes overall responsibility for the oversight and leadership of research activity planning and execution. He also takes primary responsibility for the writing of the manuscript.

Conflicts of interest

There are no conflicts to declare.

Data availability

The raw data were generated at Fukuoka University. The numerical data used to generate each graph are summarized in tabular form in the supplementary information (SI). Due to the large volume of data, some datasets cannot be presented in tabular form and are therefore provided only as SI files. These data are available from the corresponding author, Jun Kubota, upon reasonable request. Supplementary information is available. See DOI: https://doi.org/10.1039/d5se01657f.

References

1 International Energy Agency (IEA), *Renewables 2025 Analysis and Forecasts to 2030*, Paris, France, 2025.
2 Renewable Energy Policy Network for the 21st Century (REN21), *Renewables 2025 Global Status Report*, REN21 Headquarters, Bonn, Germany, 2025.
3 F. Ueckerdt, C. Bauer, A. Dirnaichner, J. Everall, R. Sacchi and G. Luderer, *Nat. Clim. Change*, 2021, **11**, 384–393.
4 H. Singh, C. Li, P. Cheng, X. Wang and Q. Liu, *Energy Adv.*, 2022, **1**, 580–605.
5 International Energy Agency (IEA), *The Role of E-Fuels in Decarbonising Transport*, Paris, France, 2023.
6 A. Nemmour, A. Inayat, I. Janajreh and C. Ghenai, *Int. J. Hydrogen Energy*, 2023, **48**, 29011–29033.
7 J. Ghandhi, M. Günthner and R. Novella, *Int. J. Engine Res.*, 2022, **23**, 707–708.
8 M. Gattrell, N. Gupta and A. Co, *J. Electroanal. Chem.*, 2006, **594**, 1–19.
9 R. J. Lim, M. Xie, M. A. Sk, J.-M. Lee, A. Fisher, X. Wang and K. H. Lim, *Catal. Today*, 2014, **233**, 169–180.
10 S. Nitopi, E. Bertheussen, S. B. Scott, X. Liu, A. K. Engstfeld, S. Horch, B. Seger, I. E. L. Stephens, K. Chan, C. Hahn, J. K. Nørskov, T. F. Jaramillo and I. Chorkendorff, *Chem. Rev.*, 2019, **119**, 7610–7672.
11 D. Sun, X. Xu, Y. Qin, S. P. Jiang and Z. Shao, *ChemSusChem*, 2019, **13**, 39–58.
12 R. Küngas, *J. Electrochem. Soc.*, 2020, **167**, 0044508.
13 N. Ullah, S. S. Shah, M. H. Suliman, F. Ismail, S. Kaci, N. A. S. Amin and M. Usman, *Energy Fuels*, 2025, **39**, 19614–19646.
14 Y. Hori, A. Murata and R. Takahashi, *J. Chem. Soc., Faraday Trans. 1*, 1989, **85**, 2309–2326.
15 Y. Seki, M. Nakabayashi, M. Sugiyama and T. Minegishi, *ChemElectyroChem*, 2025, **12**, e202400536.
16 J. Kubota and T. Okumura, *Sustain. Energy Fuels*, 2021, **5**, 935–940.
17 J. Kubota, T. Okumura and R. Hayashi, *Sustain. Energy Fuels*, 2022, **6**, 1362–1372.
18 R. Sagara, R. Hayashi, A. Hirata, S. Nagaishi and J. Kubota, *Sustain. Energy Fuels*, 2023, **7**, 5336–5341.
19 K. Imamura and J. Kubota, *Sustain. Energy Fuels*, 2019, **3**, 1406–1417.
20 S. Nagaishi, R. Hayashi, A. Hirata, R. Sagara and J. Kubota, *Sustain. Energy Fuels*, 2024, **8**, 914–926.
21 G. Han, G. Li and Y. Sun, *JACS Au*, 2024, **4**, 328–343.
22 S. Saeidi, N. A. S. Amina and M. R. Rahimpour, *J. CO_2 Utilization*, 2014, **5**, 66–81.
23 W. Li, H. Wang, X. Jiang, J. Zhu, Z. Liu, X. Guo and C. Song, *RSC Adv.*, 2018, **8**, 7651–7669.
24 W. K. Fan and M. Tahir, *J. Environ. Chem. Eng.*, 2021, **9**, 105460.
25 J. Niu, H. Liu, Y. Jin, B. Fan, W. Qi and J. Ran, *Int. J. Hydrogen Energy*, 2022, **47**, 9183–9200.
26 G. Zhang, A. Bogaerts, J. Ye and C. Liu, *Advances in CO_2 Utilization: from Fundamentals to Applications (Green Chemistry and Sustainable Technology)*, Springer, Singapore, 2024.
27 P. Qiu, S. Sun, X. Yang, F. Chen, C. Xiong, L. Jia and J. Li, *Int. J. Hydrogen Energy*, 2021, **46**, 25208–25224.
28 I. Aznam, A. Muchtar, M. R. Somalu, N. A. Baharuddin and N. A. H. Rosli, *Chem. Eng. J.*, 2023, **471**, 144751.
29 S. S. Rathore, S. Biswas, D. Fini, A. P. Kulkarni and S. Giddey, *Int. J. Hydrogen Energy*, 2021, **46**, 35365–35384.
30 H. Lee, J. Baek and M. Choi, *J. Mater. Chem. A*, 2025, **13**, 20080–20103.
31 W. J. Lee, C. Li, H. Prajitno, J. Yoo, J. Patel, Y. Yanga and S. Lim, *Catal. Today*, 2021, **368**, 2–19.
32 R. Sagara, R. Hayashi, A. Hirata, S. Nagaishi and J. Kubota, *Energy Adv.*, 2024, **3**, 1265–1270.
33 R. Sagara, E. Watanabe and J. Kubota, *Sustain. Energy Fuels*, 2025, **9**, 2658–2669.
34 H. W. Otto and R. P. Seward, *J. Chem. Eng. Data*, 1964, **9**, 507–508.
35 E. Al-Muslih, P. J. Iredale and J. K. Maund, *J. Chem. Eng. Data*, 1983, **28**, 245–246.
36 S. D. Ebbesen, S. H. Jensen, A. Hauch and M. B. Mogensen, *Chem. Rev.*, 2014, **114**, 10697–10734.
37 J. Yang, H. Muroyama, T. Matsui and K. Eguchi, *J. Power Sources*, 2014, **245**, 277–282.
38 A. Badgett, M. Ruth and B. Pivovar, *Hydrogen Production by Water Electrolysis*, eds. T. Smolinka and J. Garche, Elsevior, Amsterdam, 2022, ch 10.
39 K. M. Busam, S. P. Vudata, W. Li and F. V. Lima, *Ind. Eng. Chem. Res.*, 2025, **64**, 11129–11152.
40 K. Kobayashi and T. S. Suzuki, *Electrochem.*, 2021, **89**, 218–222.
41 T. Norby, *Solid State Ionics*, 1999, **125**, 1–11.
42 K. Saito and M. Yashima, *Nature Commun.*, 2023, **14**, 7466.
43 N. Jemaa, B. P. A. Grandjean and S. Kaliaguine, *Can. J. Chem. Eng.*, 1995, **73**, 405–410.
44 M. Vadrucci, F. Borgognoni, A. Moriani, A. Santucci and S. Tosti, *Int. J. Hydrogen Energy*, 2013, **38**, 4144–4152.
45 Atom Work, *NIMS Materials Data Platform (MDPF)*, National Institute for Materials Science, NIMS, Japan, 2025, Dec 1.
46 C. Suryanarayana and M. G. Norton, *X-Ray Diffraction: A Practical Approach*, Springer Nature, 1998.
47 T. N. Dinhová, O. Bezkrovnyi, L. Piliai, I. Khalakhan, S. Chakraborty, M. Ptak, P. Kraszkiewicz, M. Vaidulych, M. Mazur, S. Vajda, L. Kepinski, M. Vorochta and I. Matolínová, *J. Phys. Chem. C*, 2025, **129**, 1746–1757.
48 V. Mazzieri, F. Coloma-Pascual, A. Arcoya, P. C. L'Argentière and N. S. Fígoli, *Appl. Surf. Sci.*, 2003, **210**, 222–230.